

Disodium Rhodizonate/Reduced Graphene Oxide-Sodium Alginate Composite as a Cathode Material for Sodium-ion Batteries with High Cyclic Performance

Shicheng Tang¹, Zewei Yuan³, Xiangyu Deng¹, Yue Huang¹, Guodong Jiang^{1,2},
Jian Xiong^{1,2}, Han Wu¹, Songdong Yuan^{1,2,*}

¹ Hubei Collaborative Innovation Center for High-efficiency Utilization of Solar Energy, Hubei University of Technology, Wuhan, 430068, China.

² The Synergistic Innovation Center of Catalysis Materials of Hubei Province, Wuhan 430068, China.

³ Department of Chemistry, University of Amsterdam, Science Park904, 1098XH, Amsterdam, Netherlands

*E-mail: yuansongdong@aliyun.com

Received: 4 October 2020 / Accepted: 25 December 2020 / Published: 31 January 2021

Organic electrode materials have great application potential in sodium-ion batteries, but solving the cycling performance of organic materials at high current densities is a huge challenge. Here, Na₂C₆O₆/reduced graphene oxide-sodium alginate (SR/RGO-SA) was prepared by antisolvent precipitation and solvothermal methods. The hydrogen bonds formed between SR and RGO-SA and the conductive network of RGO-SA were used to prevent the capacity attenuation caused by pulverization upon prolonged cycling. Versus SR electrodes, the SR/RGO-SA electrode has better cycle performance and rate performance at high current densities. The SR/RGO-SA cathodes (7 : 3) show high specific capacity (157.2 mAh g⁻¹ at 500 mA g⁻¹ rate, 0.5–3.2 V) after 100 cycles. This modification method improves cycling performance by improving organic electrode materials.

Keywords: sodium-ion battery; disodium rhodizonate; reduced graphene oxide; sodium alginate; cathode material

1. INTRODUCTION

Cheap and large-scale energy storage technologies are essential for sustainable development of uncontrollable energy such as wind energy and solar energy [1-4]. Na⁺ has a similar electrochemical potential to Li⁺ but also offers low cost and abundant earth reserves, which makes sodium-ion batteries (SIBs) a promising energy storage technology. Just like the layered lithiated transition metal oxides in lithium-ion batteries, layered metal oxides and polyanionic compounds are the most widely studied

materials in SIBs. However, the radius of Na^+ is slightly larger than that of Li^+ , which means the insertion/extraction energies of Na^+ may increase significantly and even destroy the crystalline structure of the electrode materials [5-7]. Therefore, finding better cathode materials is the focus for SIBs. Concurrently, the production costs and recyclability of materials are also critical factors to take into account, considering the economic benefits and environmental protection.

In recent years, organic compounds, especially carbonyl compounds, have received widespread attention in cathode materials for SIBs due to their high theoretical specific capacity, rich variety, and recyclable properties [8,9]. For example, $\text{C}_6\text{Cl}_4\text{O}_2$ (tetrachloro-1,4-benzoquinone) and $\text{Na}_4\text{C}_8\text{H}_2\text{O}_6$ (2,5-dihydroxyterephthalic acid) can be used as cathode materials for SIBs and have high theoretical specific capacities of 214 and 190 mAh g^{-1} [10,11]. The high energy density of the organic compounds mainly depends on redox-active sites in the material and the molecular weight of the material [12]. Although the organic compounds have great potential as electrode materials for SIBs, most of the reported organic materials have been studied at low current densities. Organic compounds are usually prone to dissolving in organic electrolyte solutions and have low electrical conductivity, leading to a capacity that is much lower than that of other materials at higher current densities. Increasing the diffusion rates of Na^+ and electrons in organic cathode materials is an effective method to improve the high-rate capacity of the materials [13,14].

There is a four-electron redox reaction in disodium rhodizonate (SR) when it is used as a cathode material for SIBs, resulting in a theoretically high theoretical specific capacity (Figure 1a) [15]. However, the reversibility of SR fades rapidly under high rates due to the kinetic barriers that depend on the size of SR and conductivity of the electrode. In order to overcome the kinetic barriers, SR will self-smash into smaller pieces, which makes it easy to lose contact with SR as a current collector. Current methods to improve the electrochemical performance of SR are mainly choosing different adhesives or changing the size and appearance of the material [16-19].

Sodium alginate contains abundant hydroxyl groups, and it can be used as a gel to adsorb the benzoquinones in water [20,21]. Graphene with a strong conductive network and large A conjugated porous frameworks is widely used to improve the electrochemical performance of organic materials especially carbonyl compounds [22,23]. Here, disodium rhodizonate/reduced graphene oxide-sodium alginate (SR/RGO-SA) was prepared by antisolvent precipitation process and solvothermal process. There are many oxygen-containing functional groups, such as $\text{C}=\text{O}$ and $-\text{OH}$, in graphene oxide, SA, and SR, which may form hydrogen bonds with each other, resulting in cross-linking between SR, graphene oxide, and SA during the antisolvent precipitation process. Finally, graphene oxide is reduced by the solvothermal process, which ensures the conductivity of SR/RGO-SA. The architecture of SR/RGO-SA is a sheet structure in which the SR is adsorbed on the reduced graphene oxide (RGO) sheet through sodium alginate (SA). Hydrogen bonding between SA and SR mitigates pulverization-induced capacity decay (Figure 1b), but RGO maintains high electrical conductivity for the whole electrode, satisfying the kinetics requirements for the electrochemical cycle. The charge-discharge behaviors of SR/RGO-SA electrodes are similar to those of SR, but the electrochemical performance of SR/RGO-SA electrodes is much better than that of SR electrodes. Versus the SR, the SR/RGO-SA shows a high specific capacity (157.2 mAh g^{-1} at 500 mA g^{-1} rate, 0.5–3.2 V) after 100 cycles.

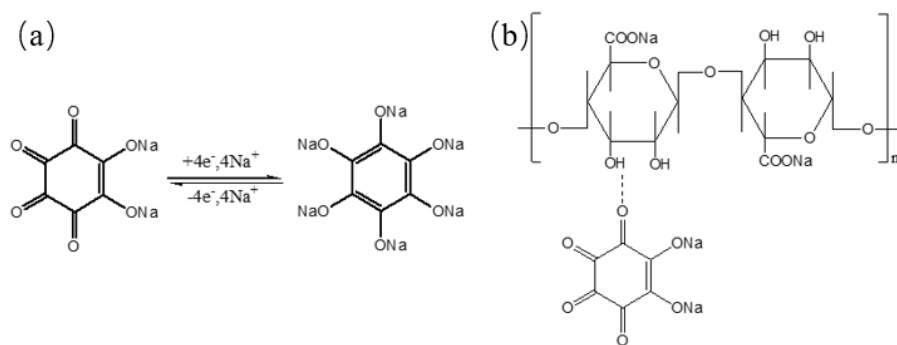


Figure 1. (a) The four-electron redox reaction for SR during charge-discharge cycles; (b) Schematic illustration of hydrogen bonding between SR and SA.

2. EXPERIMENT

2.1 Preparation of graphene oxide by the Hummers method

Here, 1 g graphite and 0.5 g $NaNO_3$ was added to 23 ml H_2SO_4 . Next, 3 g $KMnO_4$ was added slowly with stirring for 2 h at low temperature ($\leq 10^\circ C$). The temperature was raised to $35^\circ C$, and the solution was stirred for 0.5 h. After the addition of 100 mL cooled deionized water, the system temperature was rapidly increased to $90^\circ C$, and the solution was stirred for 0.5 h. Next, 40 ml H_2O_2 (10%) and 60 ml water were added to stop the reaction. After washing with deionized water to neutrality, graphene oxide was collected by vacuum filtration and freeze-drying.

2.2 Preparation of SR/RGO-SA

SR and SA were dissolved in deionized water at $80^\circ C$, and graphene oxide was dispersed in solution by ultrasound at room temperature. The solution was added dropwise to absolute ethanol at a volume ratio of 1:5 and allowed to stand for 12 hours with subsequent hydrothermal treatment at $180^\circ C$ for 9 h. The product was collected by vacuum filtration and freeze-dried. To make sure that the conditions were the same, SR and RGO-SA were processed and collected under the same conditions.

2.3 Electrode preparation

The SR/RGO-SA and SR electrode were acquired via mixing active materials, carbon-black conductive additive (Super P), and polyvinylidene fluoride (PVDF) (8:1:1 in weight ratio) in N-methyl-2-pyrrolidone (NMP). The as-obtained wet films were then obtained by the scraping cathode materials on aluminum foil surface. The wet films were dried at $80^\circ C$ for 12 h. The aluminum foil with cathode materials was cut into a wafer with a diameter of 12 mm. The cathode layers were about 1.5 mg cm^{-2} . A type 2032 semi-battery was assembled in a vacuum glove box filled with argon gas. One hundred

microliters of electrolyte solution was added to the separator. NaPF₆ (0.6 M) in diethylene glycol dimethyl ether (DEGDME) was used as an electrolyte. The charge-discharge tests and rate tests at different current densities were conducted between 0.5 V and 3.2 V (versus Na⁺/Na) on a battery test station (Arbin Instruments, USA). Cyclic voltammetry (CV) and electrochemical impedance spectroscopy (EIS) were performed with the coin cells using an electrochemical workstation (Zahner Zennium, Germany). Cyclic voltammograms (CV) were tested at a scan rate of 0.1 mV s⁻¹, with the voltage ranging from 0.5 V to 3.2 V. Electrochemical impedance spectroscopy was performed with a 10-mV amplitude between 10 mHz and 1 MHz.

2.4 Material characterization

The morphology of SR/RGO-SA and SR was characterized by scanning electron microscopy (SEM, Hitachi SU-8010, Japan). The structure of SR/RGO-SA and SR were recorded by X-ray diffraction (XRD, PANalytical B.V. Empyrean, Netherlands) in which Cu α radiation was in the range of 2θ of 10°–80°. Functional groups and hydrogen bonds were analyzed by Fourier transform infrared spectroscopy (FTIR, Thermo Fisher Nicolet IS 50, USA).

3. RESULTS AND DISCUSSION

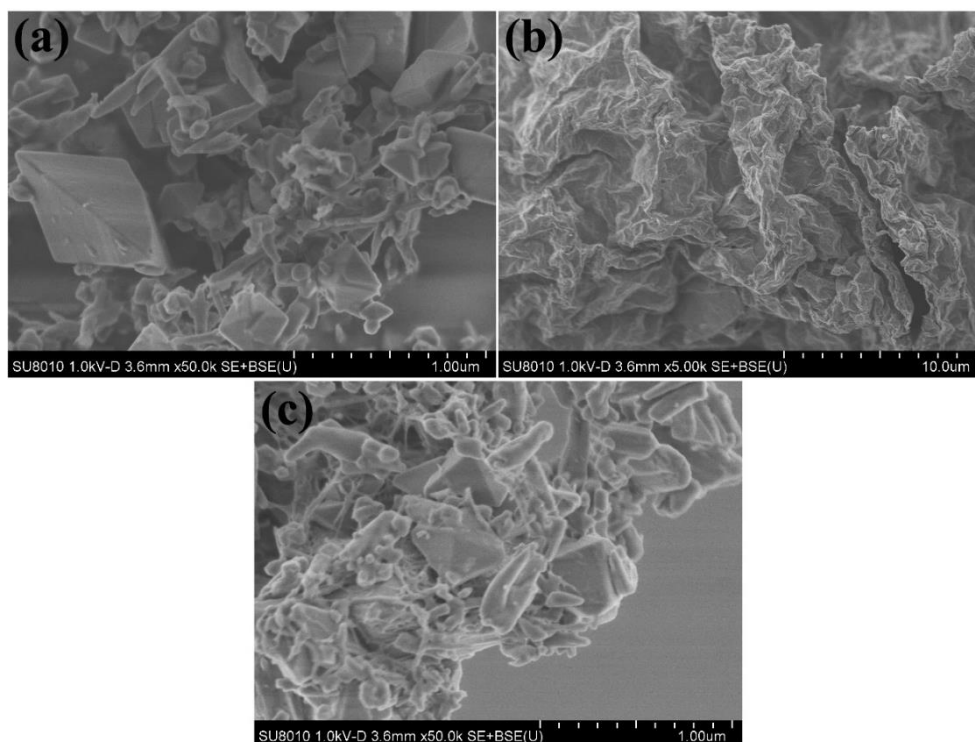


Figure 2. SEM of SR (a) and SR/RGO-SA (b); (c) SEM of SA and SR cross-linked on the surface of RGO.

Figure 2 shows SEM of SR (a) and SR/RGO-SA (b). Figure 2a shows that the SR is a nanoparticle with an octahedral crystal morphology from about 300 nm to 500 nm, which is consistent with the literature. The wrinkled nanosheets in Figure 2b are RGO because SA and SR cross-link on the surface of RGO to make it thicker than the normal RGO nanosheet. By zooming in on Figure 2b, SR and SA can be observed in Figure 2c. SR contacts closely with SA on RGO, where the octahedron is SR and the irregular particles are SA; SR and SA are connected by hydrogen bond on the RGO surface. The results show that SA and SR precipitate from deionized water at the same time in the antisolvent precipitation process and form a complete product via hydrogen bonding on the surface of graphene oxide.

Figure 3 shows the XRD of SR/SA-RGO, RGO, SA, and SR. The broad peak of RGO in 23.7° corresponds to the (002) plane that represents the interlayer distance of RGO. For SA, the broad peak at about 13.3° may represent amorphous characteristics. $\text{Na}_2\text{C}_6\text{O}_6/\text{RGO-SA}$ shows the same diffraction peaks as $\text{Na}_2\text{C}_6\text{O}_6$ at 23.0° , 26.5° , and 31.1° corresponding to the planes of (131), (311), and (400) respectively. The peak width of SR/RGO-SA in 31.1° is significantly larger than that of SR, which may be caused by the addition of RGO-SA, which reduces the SR crystal size.

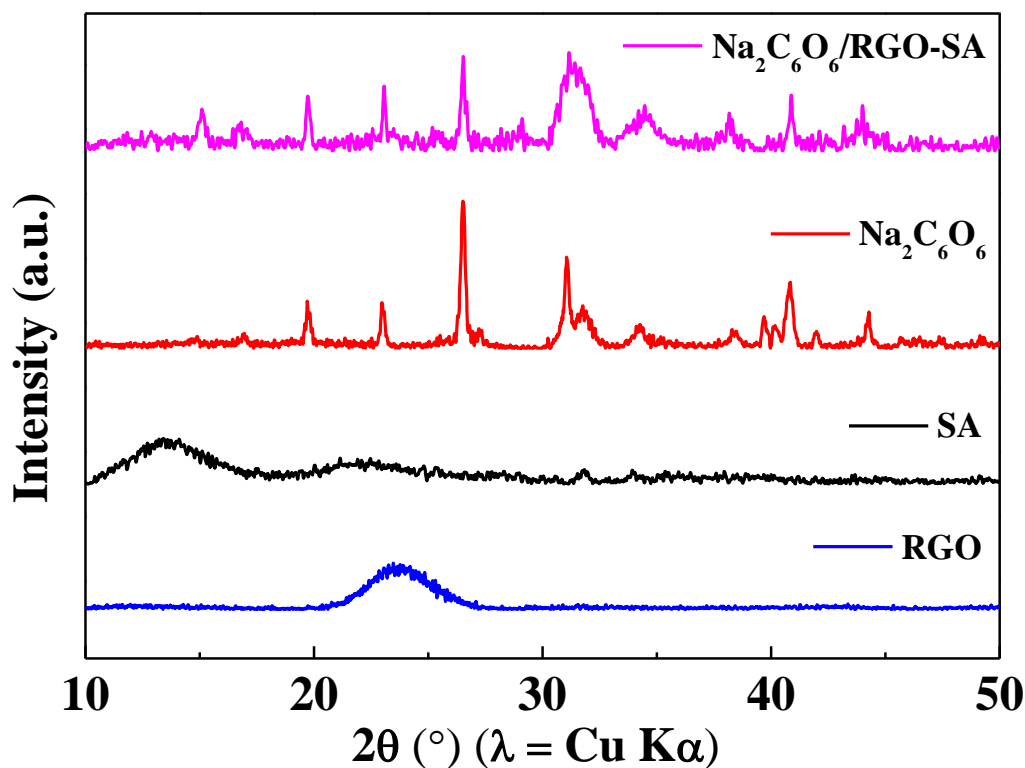


Figure 3. XRD patterns of SR/RGO-SA, SR, SA, and RGO.

FTIR analysis was used to confirm hydrogen bond formation between $\text{Na}_2\text{C}_6\text{O}_6$ and SA (Figure 4). For SR, the absorption peaks at 1649 cm^{-1} , 1523 cm^{-1} , and 1329 cm^{-1} correspond to the stretching vibration of C=O, the six-membered ring, and C-O. Several absorption bands near 1726 cm^{-1} , 1552 cm^{-1} , and 1183 cm^{-1} are still observable in RGO. The absorption bands at 1726 cm^{-1} correspond to

stretching of the C=O [24]. The bands at around 1552 cm^{-1} and 1183 cm^{-1} may be due to the skeleton vibration of RGO and C-O. The results show that the RGO still has a small amount of oxygen-containing functional groups after the solvothermal process. The broad peak formed near 3350 cm^{-1} is the stretching of the hydroxyl group, and the deformation peak of the pyran ring is at 1300 cm^{-1} in SA. For SR/RGO-SA, most of the absorption peaks of SR, SA, and RGO remained good, and the deformation peak of the pyran ring disappeared at 1300 cm^{-1} while also providing evidence for the formation of hydrogen bonds between SA and SR [25,26].

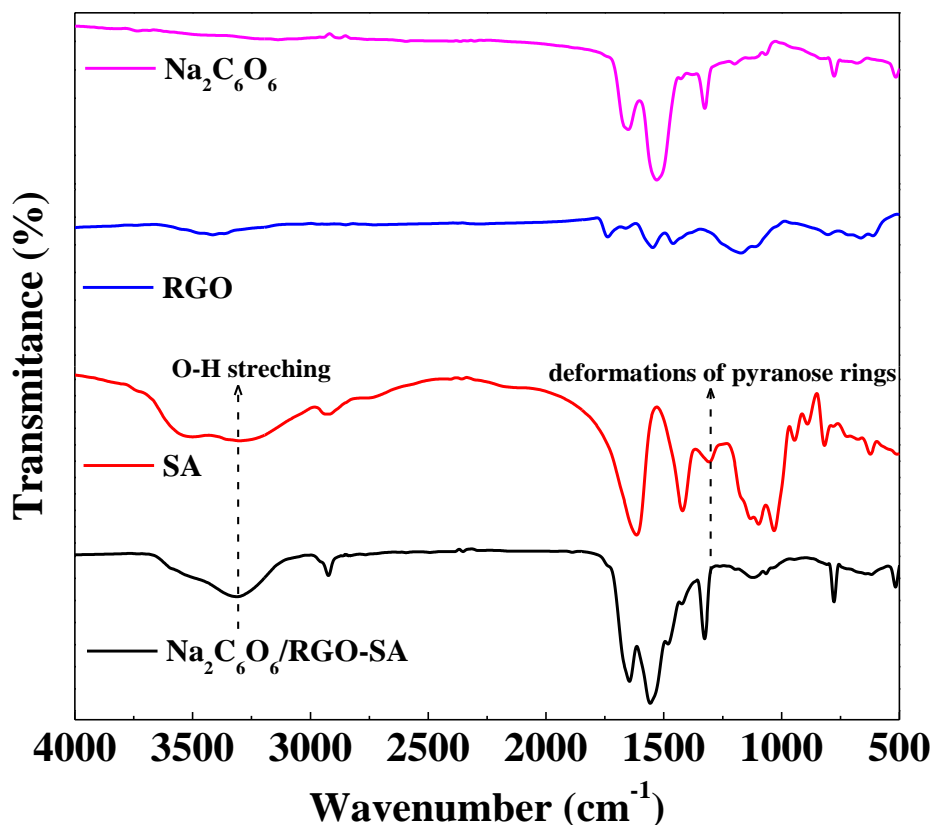


Figure 4. FTIR spectra for SR, RGO, SA, and SR-RGO-SA.

Figure 5a shows the specific capacity of the SR/RGO-SA electrode with different contents of RGO-SA at a current density of 500 mA g^{-1} . Judging from Figure 5a, the cycle performance of the SR/RGO-SA electrode increases initially and decreases afterward with increasing RGO-SA content. The discharge capacity of the SR/RGO-SA electrode ($m_{\text{SR}}: m_{\text{RGO-SA}}=7:3$) at the best mass ratio is 157.2 mAh g^{-1} after 200 cycles at 500 mA g^{-1} , while the specific capacity of the SR electrode is only 90.2 mAh g^{-1} . The reason for the increase in the specific discharge capacity of the composite may be that the hydroxyl groups on the surface of the RGO-SA form hydrogen bonds with C=O in SR, and RGO improves the conductivity of the electrodes during charge-discharge cycles, which reduces the detachment of SR after pulverization.

The galvanostatic charge-discharge curves of the SR (b) and SR/RGO-SA (c) electrode at a current density of 500 mA g^{-1} are shown in Figure 5. It is clear that the plateaus in the discharge/charge profiles of SR/RGO-SA electrode change less than those of the SR electrode at different cycles. Furthermore, the discharge/charge capacities of SR/RGO-SA electrode are higher than the specific capacity of SR electrode, suggesting synergistic effect of SR and RGO-SA. The repeatability of the galvanostatic charge-discharge curves for the SR/RGO-SA electrode underscores the stability of the battery.

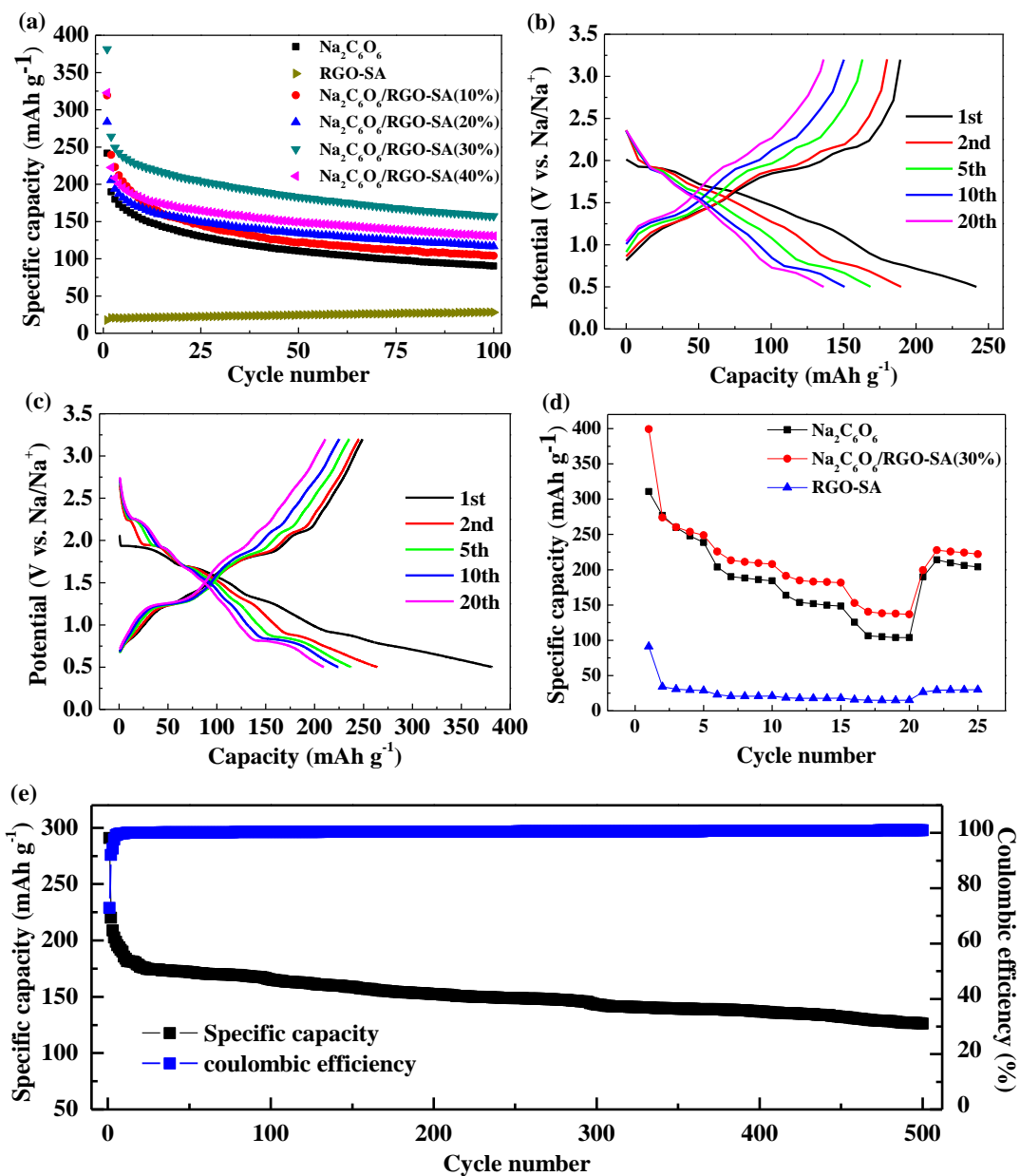
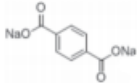
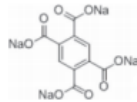
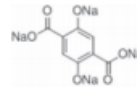
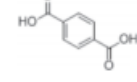


Figure 5. (a) Cycle performance of the SR-RGO-SA SR and RGO-SA electrodes at a current density of 500 mA g^{-1} . (b, c) The galvanostatic charge-discharge curves of the SR electrode (b) and the SR/RGO-SA electrode (c). (d) Rate capability of the SR/RGO-SA electrode. (e) Cyclic performance of the SR-RGO-SA SR electrodes at 1000 mA g^{-1} .

Figure 5d shows the rate performance of the SR/RGO-SA and SR electrodes. When the current density increases from 50 mA g⁻¹ to 1000 mA g⁻¹, the discharge specific capacity of the SR/RGO-SA electrode changes from 250 mAh g⁻¹ to 140 mAh g⁻¹, while the specific capacity of SR decreases from 240 mAh g⁻¹ to 100 mAh g⁻¹. After the current density returns to 50 mA g⁻¹, the discharge specific capacity of SR/RGO-SA electrode is restored to about 230 mAh g⁻¹, while the specific capacity of SR electricity is only restored to around 205 mAh g⁻¹. Therefore, the rate test results show that SR-RGO-SA electrodes have better electrochemical performance. Table 1 presents the values of electrochemical performance for sodium-ion batteries. For comparison, the SR/RGO-SA cathode material has excellent electrochemical properties compared with other materials under high current density.

Table 1. Performance comparison of Na₂C₆O₆/RGO-SA with previous works.

| | Current density(mA/g) | Cycle | Capacity(mAh/g) | Retention | Reference |
|---|-----------------------|-------|-----------------|-----------|-----------|
| Na ₂ C ₆ O ₆ /RGO-SA | 1000 | 500 | 137 | 62 % | This work |
| Na ₂ C ₆ O ₆ -PANI | 500 | 50 | 174 | 63 % | [33] |
| Na ₂ C ₆ O ₆ -RGO | 372 | 30 | 162 | 60 % | [34] |
| Na ₂ C ₆ O ₆ Nanorods | 500 | 5 | 140 | / | [35] |
|  | 10 | 50 | 203 | 80 % | [36] |
|  | 20 | 20 | 131 | 42 % | [36] |
|  | 18 | 100 | 143 | 76 % | [37] |
|  | 12 | 50 | 172 | 53 % | [36] |

SR/RGO-SA electrode also delivers good long cycle stability at high current density. As shown in Figure 5e, the discharge specific capacity of SR-RGO-SA electrodes remained at 137 mAh g⁻¹ after 500 cycles at 1000 mA g⁻¹. It is clear that the SR/RGO-SA electrode exhibits a higher reversible capacity compared to SR and RGO-SA electrode as well as those reported for other organic electrode materials for sodium-ion batteries.

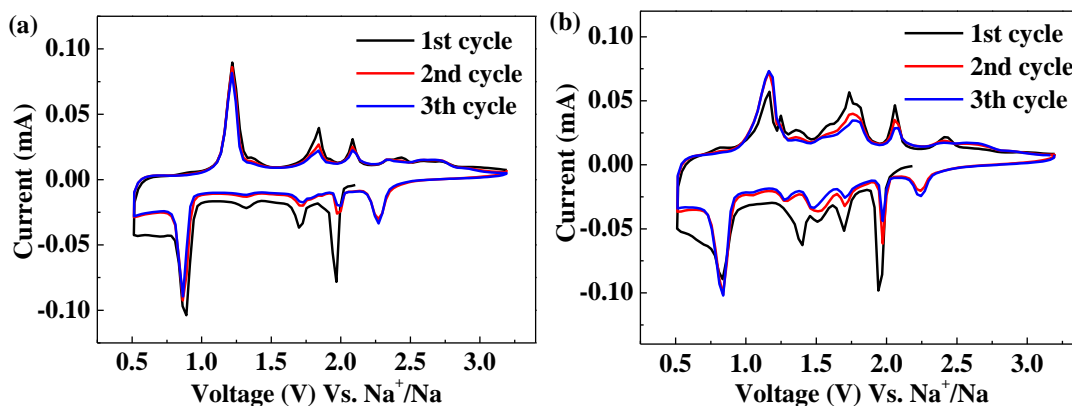
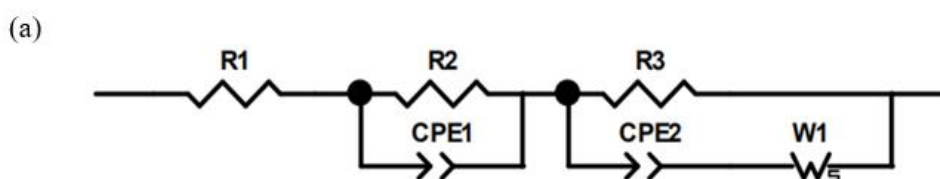


Figure 6. Cyclic voltammograms of the SR electrode (a) and the SR/RGO-SA electrode (b).

Figure 6 is the cyclic voltammetry curves of SR (a) and SR/RGO-SA (b) electrode at 0.1 mV s^{-1} . In the SR electrode, the discharging process undergoes a one-electron oxidation processes at 2.3, 2.0, 1.7, and 0.8 V, which correspond to a one-electron reduction processes at 1.2, 1.8, 2.1, and 2.5 V in the charging process [27-29]. The discharge platforms at 2.0, 1.7, and 0.9 V correspond to the formation of $\gamma\text{-Na}_3\text{C}_6\text{O}_6$, $\gamma\text{-Na}_4\text{C}_6\text{O}_6$, and $\gamma\text{-Na}_5\text{C}_6\text{O}_6$. The first discharge platform at 2.3 V corresponds to $\alpha\text{-Na}_2\text{C}_6\text{O}_6$ converted to $\text{Na}_{2.5}\text{C}_6\text{O}_6$ ($\text{Na}_{2.5}\text{C}_6\text{O}_6$ is depicted in the form of a mixture of $\alpha\text{-Na}_2\text{C}_6\text{O}_6$ and $\gamma\text{-Na}_3\text{C}_6\text{O}_6$).

There is a wide charging platform at 2.5 V in the cyclic voltammetry curves of SR electrode, which corresponds to the conversion of $\text{Na}_{2.5}\text{C}_6\text{O}_6$ to $\alpha\text{-Na}_2\text{C}_6\text{O}_6$ during the cycles. The reason for the appearance of this charging platform is that there is a kinetic barrier between $\gamma\text{-Na}_3\text{C}_6\text{O}_6$ to $\alpha\text{-Na}_2\text{C}_6\text{O}_6$ phase transformation, and this kinetic barrier is caused by the size and conductivity of the material. Because of the kinetic barrier, Na^+ cannot completely extract from $\gamma\text{-Na}_3\text{C}_6\text{O}_6$ at 2.5 V [30-32]. The kinetic barrier is overcome when the charging voltage continues to rise so that $\gamma\text{-Na}_3\text{C}_6\text{O}_6$ is completely reduced to $\alpha\text{-Na}_2\text{C}_6\text{O}_6$.

The cyclic voltammetry curves of the SR/RGO-SA electrode are consistent with the SR electrode. There is a discharging platform at 1.5 V that corresponds to the $\gamma\text{-Na}_3\text{C}_6\text{O}_6$ on the surface of active material reduced to $\gamma\text{-Na}_4\text{C}_6\text{O}_6$. The strain caused by Na^+ intercalation is increased due to the formation of hydrogen bonds between $\gamma\text{-Na}_3\text{C}_6\text{O}_6$ and RGO-SA on the surface of active materials. This leads to a large potential lag. As a result, the reduction potential of $\gamma\text{-Na}_3\text{C}_6\text{O}_6$ on the surface of active materials is lower than that of normal $\gamma\text{-Na}_3\text{C}_6\text{O}_6$. The charging platform of 2.5 V in SR/RGO-SA is more obvious than that of SR during the cycle, which shows that the addition of RGO and SA may affect the electrochemical behavior.



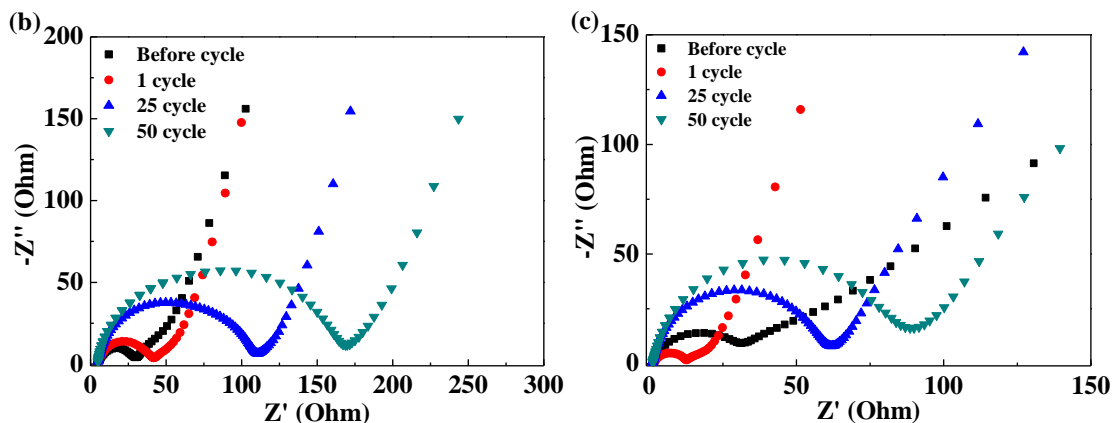


Figure 7. (a) The equivalent circuit for the EIS fitting of the SR electrode and SR-RGO-SA electrode; Nyquist plots of the SR electrode (b) and SR-RGO-SA electrode (c).

Table 2. Rct results from SR electrode and SR-RGO-SA electrode after fitting.

| R _{ct} (Ω) | before | 1 | 25 | 50 |
|---|--------|------|-------|-------|
| Na ₂ C ₆ O ₆ | 23.3 | 40.4 | 104.1 | 155.0 |
| SR/RGO-SA | 25.0 | 11.1 | 63.7 | 90.1 |

Figure 7a shows the equivalent circuit of the electrochemical impedance spectroscopy of the SR electrode (b) and SR/RGO-SA electrode (c). The R_{sol} , R_{SEI} , and R_{ct} represent the Ohmic, interface resistance, and charge transfer resistances, respectively. The interface resistance is related to the SEI layer. CPE represents the constant phase element, and W_s is the Warburg resistance. CPE_1 is related to the capacitive behavior at the interface, and CPE_2 is related to the capacitive behavior of the electrodes. A Nyquist plot of SR/RGO-SA and SR electrodes consists of a semi-circle in a high-frequency region and an oblique line in low-frequency regions. Semi-circles represent the Na^+ passing through the SEI layer and charge transfer of the material, while the size of the semi-circle reflects the impedances of interface and charge transfer. R_{ct} results at different charge-discharge cycles from SR/RGO-SA and SR electrodes are shown in Table 2. After the 1st cycle, the charge transfer resistance of the SR electrode increased from 23.3 to 40.4 Ω whereas the resistance of the SR/RGO-SA electrode decreases from 25.0 Ω to 11.1 Ω. In the SR electrodes, SR would be pulverized during the first cycle, and the SR that had been pulverized had insufficient contact with the current collector resulting in an increase in R_{ct} .

For the SR-RGO-SA electrodes, the hydrogen bonds formed between RGO-SA and pulverized SR lead to high-conductivity RGO and could maintain the conductivity of the SR/RGO-SA electrode. However, the pulverization produces more surface area of SR, which enables better contact between the SR and the current collector. Therefore, the R_{ct} of the SR/RGO-SA electrode decreases after the 1st cycle. After the 50th cycle, the charge transfer resistance of SR electrode increases from 23.3 to 155 Ω, whereas the resistance of the SR/RGO-SA electrode increases from 25.0 to 90.1 Ω. This shows that the addition of RGO-SA can reduce the increase in the charge transfer resistance caused by the pulverization of SR during the charge-discharge cycles.

4. CONCLUSIONS

In summary, SR/RGO-SA was fabricated from SR by antisolvent precipitation and solvothermal methods and applied for sodium-ion batteries for the first time. Versus SR electrodes, the SR/RGO-SA electrodes exhibit a high reversible capacity and cyclic performance through electrochemical tests. When the amount of RGO-SA is 30 wt%, the Na₂C₆O₆/RGO-SA electrode has the best cycle performance. Versus the original Na₂C₆O₆ electrode, the Na₂C₆O₆/RGO-SA electrode can still release 137 mAh g⁻¹ specific discharge capacity after 500 cycles at a current density of 1000 mA g⁻¹. The excellent electrochemical performance of SR/RGO-SA is attributed to the synergistic effect of RGO, SA, and SR. In SR/RGO-SA, the addition of RGO can also favor fast electron transport. Therefore, the electrochemical performance of the SR/RGO-SA electrode may be a method to improve the cycling performance of organic sodium-ion batteries.

Table 1 shows the cyclic properties of Na₂C₆O₆-related modified materials and organic anode materials of sodium ion batteries with similar structure are shown. Na₂C₆O₆/RGO-SA cathode material has excellent electrochemical properties compared with other materials under high current density. Compared with other modification methods of Na₂C₆O₆, the composite prepared in this paper has excellent cycling performance under high current density.

ACKNOWLEDGMENTS

This work was financially supported by International Science & Technology Cooperation Program of China (2016YFE0124300), Major Technological Innovation Projects in Hubei Province (2018AAA056), and Foundation of the Hubei Collaborative Innovation Center for High-efficiency Utilization of Solar Energy (HBSDY201702 and HBSKFZD2017006).

COMPLIANCE WITH ETHICAL STANDARDS

Conflict of interest: The authors declare that they have no conflict of interest.

References

1. T. M. Gür, *Energy Environ. Sci.*, 11 (2018) 2696.
2. B. Dunn, H. Kamath and J. M. Tarascon, *Science*, 334 (2011) 928.
3. D. Kundu, E. Talaie, V. Duffort and L. F. Nazar, *Angew. Chem. Int. Ed.*, 54 (2015) 3431.
4. D. Larcher and J. M. Tarascon, *Nat. Chem.*, 7 (2015) 19.
5. S. Y. Liu, X. Liu, T. Wang, L.-Z. Fan and L. Jiao, *Sustainable Energy Fuels*, 1 (2017) 986.
6. H. Kim, H. Kim, Z. Ding, M. H. Lee, K. Lim, G. Yoon and K. Kang, *Adv. Energy Mater.*, 6 (2016) 1600943.
7. M. D. Slater, D. Kim, E. Lee and C. S. Johnson, *Adv. Funct. Mater.*, 23 (2013) 947.
8. T. B. Schon, B. T. McAllister, P. F. Li and D. S. Seferos, *Chem. Soc. Rev.*, 45 (2016) 6345.
9. B. Häupler, A. Wild and U. S. Schubert, *Adv. Energy Mater.*, 5 (2015) 1402034.
10. S. Wang, L. Wang, Z. Zhu, Z. Hu, Q. Zhao and J. Chen, *Angew. Chem. Int. Ed.*, 53 (2014) 5892.
11. R. B. Araujo, A. Banerjee and R. Ahuja, *J. Phys. Chem. C*, 121 (2017) 14027.
12. H. Kim, J. E. Kwon, B. Lee, J. Hong, M. Lee, S. Y. Park and K. Kang, *Chem. Mater.*, 27 (2015) 7258.
13. K. C. Kim, *Ind. Eng. Chem. Res.*, 56 (2017) 12009.

14. Y. Lu, Q. Zhang, L. Li, Z. Niu and J. Chen, *Chem*, 4 (2018) 2786.
15. K. Chihara, N. Chujo, A. Kitajou and S. Okada, *Electrochim. Acta*, 110 (2013) 240.
16. J. Gu, Y. Gu and S. Yang, *Medchemcomm*, 53 (2017) 12642.
17. C. Luo, X. Fan, Z. Ma, T. Gao and C. Wang, *Chem*, 3 (2017) 1050.
18. C. Wang, Y. Fang, Y. Xu, L. Liang, M. Zhou, H. Zhao and Y. Lei, *Adv. Funct. Mater.*, 26 (2016) 1777.
19. Y. Wang, Y. Ding, L. Pan, Y. Shi, Z. Yue, Y. Shi and G. Yu, *Nano Lett.*, 16 (2016) 3329.
20. Z. Luo, H. Chen, S. Wu, C. Yang and J. Cheng, *Chemosphere*, 237 (2019) 124493.
21. Y. X. Ma, X. Li, W. J. Shao, Y. L. Kou, H. P. Yang and D. J. Zhang, *J. Nanosci. Nanotechnol.*, 20 (2020) 2205.
22. D. Wu, H. Li, R. Li, Y. Hu and X. Hu, *Medchemcomm*, 54 (2018) 11415.
23. C. Yuan, Q. Wu, Q. Li, Q. Duan, Y. Li and H.-g. Wang, *ACS Sustainable Chem. Eng.*, 6 (2018) 8392.
24. Y. Lu, X. Hou, L. Miao, L. Li, R. Shi, L. Liu and J. Chen, *Angew. Chem. Int. Edit.*, 58 (2019) 7020.
25. S. K. Papageorgiou, E. P. Kouvelos, E. P. Favvas, A. A. Sapalidis, G. E. Romanos and F. K. Katsaros, *Carbohydr. Res.*, 345 (2010) 469.
26. I. Kovalenko, B. Zdyrko, A. Magasinski, B. Hertzberg, Z. Milicev, R. Burtovyy, I. Luzinov and G. Yushin, *Science*, 334 (2011) 75.
27. Y. Huang, G. Jiang, J. Xiong, C. Yang, Q. Ai, H. Wu and S. Yuan, *Appl. Surf. Sci.*, 499 (2020) 143849.
28. J. Gu, Y. Gu and S. Yang, *ChemComm*, 53 (2017) 12642.
29. Y. Wang, Y. Ding, L. Pan, Y. Shi, Z. Yue, Y. Shi and G. Yu, *Nano Lett.*, 16 (2016) 3329
30. A. Abouimrane, W. Weng, H. Eltayeb, Y. Cui, J. Niklas, O. Poluektov and K. Amine, *Energy Environ. Sci.*, 5 (2012) 9632
31. S. Wang, L. Wang, Z. Zhu, Z. Hu, Q. Zhao and J. Chen, *Angew. Chem. Int. Ed.*, 53 (2014) 5892.
32. T. Yamashita, H. Momida and T. Oguchi, *Electrochimica Acta*, 195 (2016) 1.
33. T. Yamashita, H. Momida and T. Oguchi, *J. Phys. Soc. Jpn.*, 84 (2015) 074703.
34. M. A. Georgia, Junqueira, W. R. Rocha, W. B. De Almeida and H. F. Dos Santos, *J. Mol. Struct-Theochem.*, 684 (2004) 141.
35. C. Xia, S. L. Zhu, M. Tang and S. F. Xu, *J. Phys. Chem. C*, 122 (2018) 21185.
36. M. Lee, J. Hong, J. Lopez, Y. Sun, D. Feng, K. Lim, W. C. Chueh, M. F. Toney, Y. Cui and Z. Bao, *Nat. Energy*, 2 (2017) 861.